nature geoscience

ARTICLES

https://doi.org/10.1038/s41561-018-0126-4

Anomalous mantle transition zone beneath the Yellowstone hotspot track

Ying Zhou

The origin of the Yellowstone and Snake River Plain volcanism has been strongly debated. The mantle plume model successfully explains the age-progressive volcanic track, but a deep plume structure has been absent in seismic imaging. Here I apply diffractional tomography to receiver functions recorded at USArray stations to map high-resolution topography of mantle transition-zone discontinuities. The images reveal a trail of anomalies that closely follow the surface hotspot track and correlate well with a seismic wave-speed gap in the subducting Farallon slab. This observation contradicts the plume model, which requires anomalies in the mid mantle to be confined in a narrow region directly beneath the present-day Yellowstone caldera. I propose an alternative interpretation of the Yellowstone volcanism. About 16 million years ago, a section of young slab that had broken off from a subducted spreading centre in the mantle first penetrated the 660 km discontinuity beneath Oregon and Idaho, and pulled down older stagnant slab. Slab tearing occurred along pre-existing fracture zones and propagated northeastward. This reversed-polarity subduction generated passive upwellings from the lower mantle, which ascended through a water-rich mantle transition zone to produce melting and age-progressive volcanism.

The mantle plume model for the Yellowstone and Snake River Plain volcanism (Fig. 1) has been under much debate for several decades[1–4]. Seismically slow (hot) anomalies in the uppermost ~200 km of the mantle beneath Yellowstone and the Snake River Plain have been consistently imaged in recent tomographic studies in the western United States, but a continuous hot plume structure down to the deep mantle has been absent[5–9]. The most dominant seismic features in the mid mantle are fast (cold) anomalies associated with the subducted oceanic Farallon Plate, currently in the North American mantle transition zone (MTZ)[6–12]. The geometry of the fast anomalies indicates a strong slab fragmentation that created 'gaps' in an otherwise spatially continuous feature in tomographic images[8–12]. The absence of a continuous mantle plume down to the lower mantle in seismic images has been attributed to possible complex interactions between a narrow uprising plume beneath the Yellowstone and the massive downgoing Farallon slab in the North American mantle[3,7–10]. However, geodynamical simulations have been unsuccessful in reproducing the age migration of the volcanic track at Yellowstone in a complex subduction environment when seismic constraints are applied[4,13]. This controversy left subduction-driven mantle flows as alternative models for Yellowstone volcanism, for example, the eastward intrusion of hot Pacific mantle driven by the subduction of the Farallon Plate[13] or possible upwellings around a fragmented slab during rapid trench retreat[9].

A major 'slab gap' in seismic wave speed was first published in 2008[7] and later confirmed by other seismic studies based on data recorded at the USArray seismic network, which has provided unprecedented data coverage in the United States with an average station spacing of about 70 km. The slab gap is most evident in the MTZ in which subduction becomes stagnant just above the 660 km discontinuity and extends northeastward from the Oregon and Idaho border, roughly following the Yellowstone volcanic track. The exact cause of the slab gap was unclear, but different subduction angles have been suggested as a possible mechanism[7,10]. The size and location of the slab gap vary among different wave-speed studies because spatial resolutions in these models are generally limited to ~300 km in the MTZ and smaller structures may have not been well resolved. Teleseismic receiver functions, however, can be used to provide complementary constraints with better lateral resolution at depths of the MTZ as they utilize waves converted directly at seismic discontinuities near receivers. However, to date receiver function studies have been unable to resolve the disparity of opinion about the plume origin of the Yellowstone volcanism largely due to the limitations of back-projection imaging methods used in those studies[14–16].

Finite-frequency receiver function tomography

The mantle transition-zone discontinuities, that is, the 410 km discontinuity and the 660 km discontinuity, are associated with pressure-induced olivine phase transformations. The actual depths at which these phase transitions occur depend strongly on the temperature and water content[17,18]. In the classic plume model, the 660 km discontinuity is expected to occur at a depth shallower than 660 km, whereas the 410 km discontinuity occurs at a depth greater than 410 km. The depths of the two discontinuities can be constrained using receiver functions constructed from horizontal- and vertical-component P-wave coda seismograms because teleseismic P waves generate secondary converted S waves at the seismic discontinuities that arrive later in the P-wave coda. Traditional receiver function imaging is based on back-projection using ray theory, which breaks down for structures that are comparable to or smaller than the size of the Fresnel zone[19]. To obtain high-resolution depth variations of the two discontinuities in the western United States, I measured finite-frequency travel times of P410 and P660 receiver functions recorded at USArray Transportable Array (TA) stations and imaged the topography of the two discontinuities based on a newly developed finite-frequency tomographic theory for receiver functions[19]. Finite-frequency imaging theory is more general than ray theory as it accounts for wave diffractional effects and, therefore, can be applied to recover small-scale slab structures that are often in the order of a couple of hundred kilometres[20], which may not be resolvable in traditional receiver function analysis[19].

Department of Geosciences, Virginia Tech, Blacksburg, VA, USA. e-mail: yingz@vt.edu

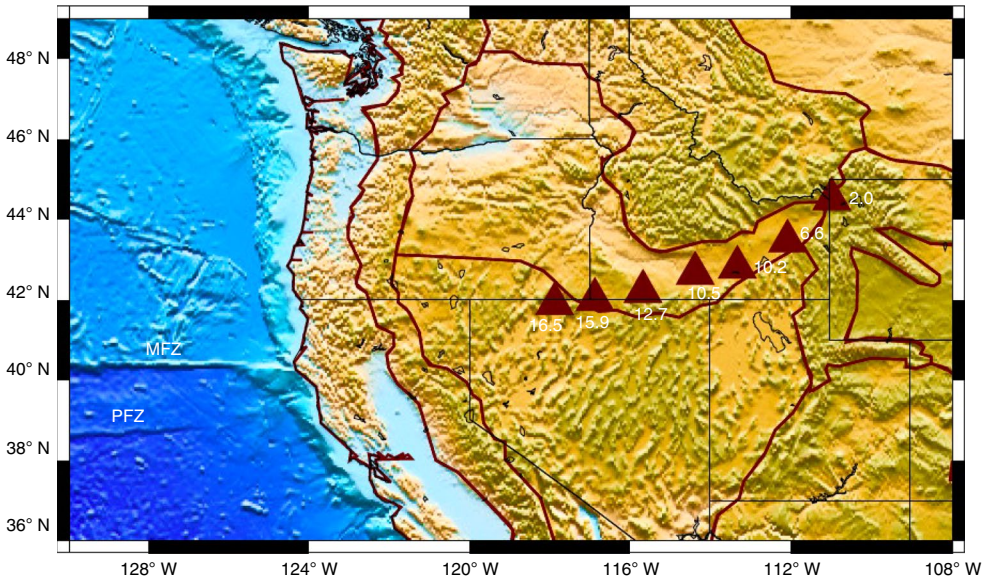

Fig. 1 | Location of the Yellowstone hotspot track. Triangles indicate general locations of the Yellowstone and Snake River Plain age-progressive volcanoes (age in millions of years), plotted on a topography map of the western United States. MFZ, Mendocino Fracture Zone; PFZ, Pioneer Fracture Zone. The dark lines indicate major geological boundaries.

The most striking feature in the high-resolution 410 km and 660 km discontinuity topography maps is a trail of anomalies beneath Yellowstone and the Snake River Plain, which extends in the northeast–southwest (NE–SW) direction and closely follows the surface volcanic track (Fig. 2). The 660 km discontinuity along this track is shallower than that in the surrounding mantle in which the associated olivine phase transformation occurs deeper than in a normal mantle, as expected in a region with a large stagnant slab near the 660 km discontinuity. If we assume that seismic anomalies in the lower MTZ are caused dominantly by temperature variations,

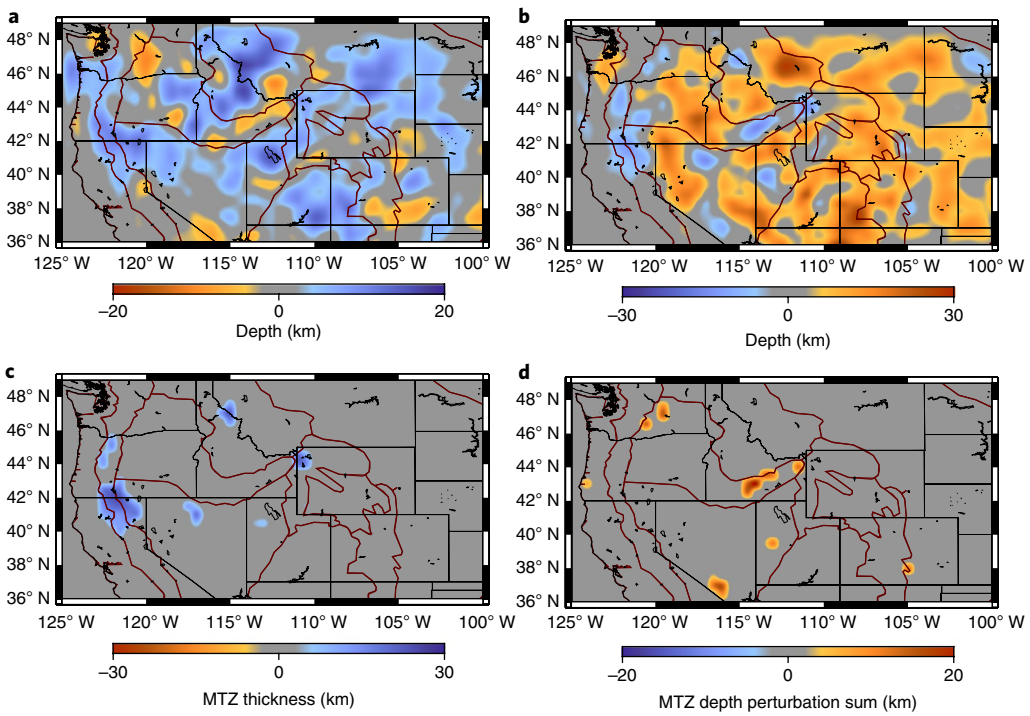

Fig. 2 | Mantle transition-zone discontinuities from receiver function diffraction tomography. a,**b**, Depth perturbations of the 660 km (**a**) and 410 km (**b**) discontinuities, respectively. **c**, Thicker MTZ where the two discontinuities are anticorrelated and perturbations are larger than uncertainties (3 km for the 660 km and 5 km for the 410 km discontinuities). The anomalies can be explained by a possible vertical slab throughout the MTZ, except for the anomaly at Yellowstone where the thicker MTZ corresponds to the trench of the reversed polarity subduction (Fig. 5). **d**, The sum of discontinuity-depth perturbations where both discontinuities are deeper, which is indicative of possible vertical upwellings through a hydrated MTZ.

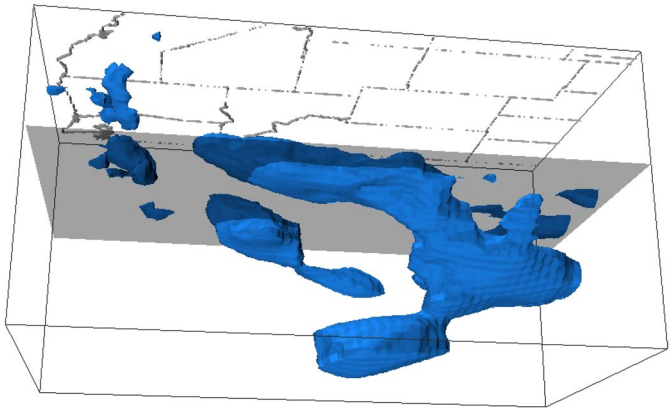

Fig. 3 | 3D rendering and re-examination of S-wave slab anomalies in the western United States. The isosurface represents 1% fast seismic wave-speed anomalies at depths from 50 km to 1,600 km (ref. [10]). US state boundaries are plotted at the surface for geographical reference. Fast anomalies in the upper mantle beneath the craton are removed for a better illustration of the slab. Map views of the same wave-speed model at different depths are plotted in Supplementary Fig. 8. The horizontal plane in grey is plotted at a 660 km depth for reference. A cartoon representation of this figure is plotted in Fig. 4d.

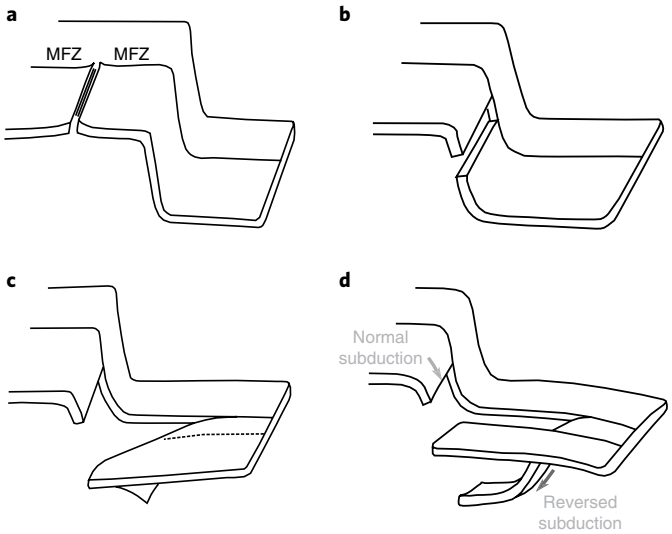

Fig. 4 | Cartoon illustration of the stages of subduction in the western United States (not to scale). a, Stagnant slab subduction >30 Ma. **b**, Ridge subduction and slab break off ~25 Ma. **c**, Reversed subduction (polarity reversal) ~16 Ma. **d**, Present-day slab geometry as seen in Fig. 3: slab tearing along the Mendocino and Pioneer Fracture Zones. For simplicity, the Pioneer Fracture Zone is not illustrated in **a** and **b** and is indicated as a dashed line in **c**.

the trail of anomalies in the 660 km discontinuity map could be explained well by a hot mantle flow rising up through a linear gap within a large slab of the cold Farallon Plate. The distribution of slab anomalies in the 660 km discontinuity map in Fig. 2 correlate well with seismic wave-speed anomalies in the MTZ, but show more detail in slab fragmentation (Supplementary Fig. 7). The width of the hotspot-track anomalies in the 660 km discontinuity model is about 150 km, narrower than the slab gap imaged in the wave-speed models, as the wave-speed models have a lower resolution at those depths due to a ~200 km grid spacing used in the model parameterization. The hotspot track at the MTZ cannot be explained by a plume model because a stationary mantle plume may only produce a volcanic track at the surface due to the movement of the rigid lithospheric plate, but not in the mid mantle.

The correlation between depth perturbations of the 410 km and the 660 km discontinuities in the western United States is overall positive, as both phase transformations occur at greater depths than in a normal mantle. The mean depths are about 416 and 663 km, respectively. This observation is largely consistent with previous receiver function studies[14,16]. I interpret this positive correlation as a result of thermal variations in the mid mantle. Although the Clapeyron slope is positive for the 410 km and negative for the 660 km, seismic anomalies suggest that the western United States is hotter (than normal) in the upper mantle but colder in the lower MTZ due to slab stagnation[7,8,10] (Supplementary Fig. 7). The depth perturbations along the Yellowstone anomaly track, however, show an opposite polarity: both the 410 km and the 660 km discontinuities are shallower than the surrounding mantle. I interpret the elevated 410 km discontinuity along the anomaly track as wet spots due to a high water solubility in the MTZ[21–23]. A hydrated layer associated with the 410 km discontinuity, and the consequential melting events, have been reported in regions in which mantle flows rise through the 410 km discontinuity[24,25]. In the western United States, the MTZ is hydrated by the stagnant oceanic Farallon slab, and the seismic attenuation structure in the western United States supports the presence of water and partial melt at those depths[10]. The anomalies at the 410 km discontinuity are at locations slightly different from those in the 660 km discontinuity map (Fig. 2). This indicates that the rising mantle flows are probably not strictly vertical.

Reversed polarity subduction of the Farallon Plate

Subduction of a large oceanic plate is one of the most spectacular and complex processes in plate tectonics. The convergence between the oceanic Farallon Plate and the North American Plate eventually led to the subduction of the youngest seafloor, including active seafloor spreading centres, into the mantle beneath the North American continent. The ridge subduction event explains the termination of arc volcanism and the development of the San Andreas strike-slip system[26]. As a result, a slab window formed and widened, and the Mendocino Triple Junction propagated northward[26,27]. Seismic structures north of the Mendocino show that slab in the upper mantle is still connected to the currently active Cascadia subduction zone Supplementary Fig. 7). To the south, slab anomalies are absent in the upper mantle where subduction ceased about 30 million years ago (30 Ma), and most slab materials have sunk down to the MTZ beneath present-day Utah (Fig. 3 and Supplementary Fig. 7), with only small volumes of fossil slab remnants in the uppermost 120 km of mantle[28]. The anomalies at the 660 km discontinuity show a northeastward subduction of an enormous Farallon oceanic plate, fragmented along subducted oceanic fracture zones (Fig. 2). If we extend the hotspot track on the discontinuity maps westward, it roughly meets the Pacific Mendocino Fracture Zone (Fig. 1). However, current plate reconstruction model predicts a trajectory of the Farallon Mendocino Fracture Zone (the 'conjugate' of the Pacific Mendocino Fracture Zone) with an orientation different from the hotspot track[8].

Based on the high-resolution discontinuity maps and a re-examination of the seismic wave-speed structure in the mid mantle at their respective resolution, I propose that the slab south of the Farallon Mendocino Fracture Zone broke off from a subducted spreading centre in the shallow mantle about 25 Ma (Fig. 4). The upper slab either stayed neutrally buoyant in the shallow 150 km of the upper mantle or was captured by the Pacific Plate[28], whereas the lower slab sank with a steep angle. The lack of strong coupling with a surface plate facilitated a fast sinking rate of about 5 cm yr^{-1} and an easier penetration through the 660 km discontinuity. This detached slab is weakly coupled to the northern slab through the Mendocino Fracture Zone, and slab tearing occurred along the fracture zone as

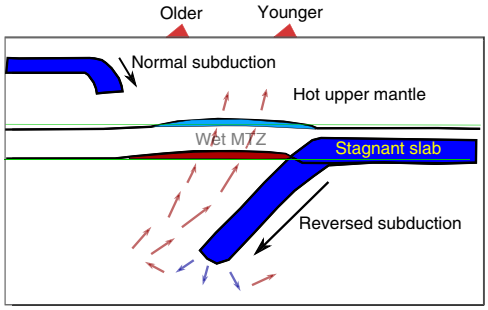

Fig. 5 | Cartoon illustration of reversed subduction (not to scale). Reversed subduction (polarity reversal) of the stagnant slab was initiated at the MTZ and generated strong upwellings that rose through a hydrated MTZ. Dehydration melting occurred across the 410 km discontinuity. This process explains the Yellowstone and Snake River Plain age-progressive volcanoes (hotspot track) as well as undulations of the MTZ discontinuities (thick lines). Two thin green lines are plotted at 410 km and 660 km depths for reference.

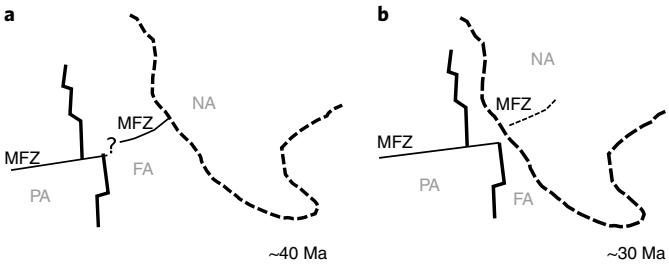

Fig. 6 | Sketch of the Pacific and Farallon fracture zones. This sketch illustrates a possible scenario that explains the difference in orientation between Pacific fracture zones and their conjugates on the subducted Farallon Plate. PA, Pacific Plate; FA, Farallon Plate; NA, North American Plate; MFZ, Mendocino Fracture Zone. The thick solid and dashed lines indicate the PA–FA and FA–NA plate boundaries, respectively. **a**, Pre-ridge subduction configuration (~40 Ma): the Pacific-Farallon Fracture Zone configuration resembles the present-day Pacific–Cocos and Pacific–Nazca system (main text). **b**, Configuration at ~30 Ma when the PA–FA mid-ocean ridge approached the FA–NA subduction boundary.

the detached southern slab sank further down to the lower mantle. The southern slab started to penetrate the 660 km discontinuity about 16 Ma, which made subduction reverse its polarity with the younger slab in the lower mantle pulling down older, stagnant slab in the MTZ (Figs. 4 and 5). The reversed polarity subduction started from the west end of the detached slab, south of the Mendocino, and propagated northeastward along the Yellowstone anomaly track. Slab tearing also occurred along the Pioneer Fracture Zone during the reversed polarity subduction, which resulted in a fragment of slab sinking deeper into the lower mantle (Figs. 2–5).

The slab tearing during reversed polarity subduction produced strong passive upwellings from the lower mantle (Fig. 5). This poloidal component of mantle flow associated with the sinking of the slab may have become more significant with increasing mantle viscosity[29]. The upwellings through the slab-hydrated MTZ contain a high water content, which facilitates dehydration melting as the flows cross the 410 km discontinuity. The melt further rises up in the superadiabatic upper mantle due to buoyancy, which leads to surface volcanism. This model explains both the lower mantle signature of the helium-3/helium-4 isotope ratios observed in the basaltic volcanism and the absence of a lower-mantle plume tail in seismic images. Seismic wave-speed structure, although with a limited lateral resolution of about 300 km at those depths, also supports an early slab breaking-off event as well as the sequential tearing and reversed polarity subduction (Fig. 3). The relation between the onset of the reversed polarity subduction and the formation of the Columbia River Flood Basalt remains unclear and requires further investigation in its geodynamics. Slab tearing in the mantle indicates that the stress conditions and physical properties are not uniform, but are strongly influenced by pre-existing structures. In general, the stagnant slab in the western United States does not show significant differences with age in both wave-speed and discontinuity models, which indicates that older (earlier) subducted materials may have warmed up due to their longer residence time in the mantle, which balances out their initial temperature differences.

The deepest subducted slab in this reversed polarity subduction has reached to about 1,200 km (with limited depth resolution), which indicates a vertical sinking speed of about 3.5 cm yr^{-1} in the lower mantle (Fig. 3 and Supplementary Fig. 8). The rest of the stagnant slab in the western United States has been gradually pulled down to about 700–800 km and dips to the east with a normal subduction polarity (Fig. 3). This indicates that, as slab tearing propagated northeastward, the pulling force associated with reversed polarity subduction became stronger, which facilitated an overall subduction mode switch of the Farallon slab from stagnating to penetrating. If we extend the Yellowstone hotspot track westward, it meets the subduction front roughly at the latitude of the Mendocino Fracture Zone about 30 Ma, assuming a northwest relative motion between the Pacific Plate and the North American Plate at a rate of about 4.5 cm yr (ref. [30]). The geometry of the stagnant slab in the MTZ indicates that subduction was at a northeast direction, different from the present-day eastward subduction (Fig. 2) and consistent with the change in plate boundary orientation associated with the extension of the basin and range.

Implications on fracture zones and plate movement

The difference in orientation between fracture zones on the North American Plate and their 'conjugates' on the subducted Farallon Plate suggests that the evolution of fracture zones on the Farallon Plate may have been a complex process (Fig. 5), possibly related to the break-up of the Farallon Plate into smaller microplates. In the Southern Pacific, where seafloor records on the remnant Farallon Plate have not been subducted, gravity and magnetic anomalies suggest a complex evolution history of the Farallon Plate[31,32]. For example, The Mendãna Fracture Zone on the Nazca Plate and the Orozco Fracture Zone on the Cocos Plate have orientations very different from their conjugates on the Pacific Plate due to the formation and rotation of a short-lived Bauer microplate and re-orientation of the East Pacific Rise. In our model (Fig. 6), slab tearing and hotspot track occurred along fracture zones on the Farallon Plate. The slab window, on the other hand, would have been influenced by the configuration of the Pacific Plate, which includes the Pacific fracture zones and the migration of the Mendocino Triple Junction[26,27].

The close proximity between the anomaly track in the MTZ and locations of the surface Neogene volcanism indicates that the absolute movement of the North American Plate in the past 16 million years was 1–2 cm yr^{-1} or less. This rate is comparable to the the seafloor-spreading rate in the North Atlantic Ocean and much smaller than estimates obtained from caldera locations using a simple mantle plume model[33]. In global reconstruction models, the absolute plate motion of the North American Plate varies between 1 cm yr^{-1} and 2.5 cm yr^{-1} depending on the reference frame[34], in general agreement with our model.

Methods

Methods, including statements of data availability and any associated accession codes and references, are available at https://doi.org/10.1038/s41561-018-0126-4.

Received: 10 October 2017; Accepted: 13 April 2018;
Published online: 21 May 2018

References

1. Morgan, W. J. Deep mantle convection plumes and plate motions. *Bull. Am. Assoc. Pet. Geol.* **56**, 203–213 (1972).
2. Christiansen, R. L., Foulger, G. R. & Evans, J. R. Upper-mantle origin of the Yellowstone hotspot. *Geol. Soc. Am. Bull.* **114**, 1245–1256 (2002).
3. Kincaid, C., Druken, K. A., Griffiths, R. W. & Stegman, D. R. Bifurcation of the Yellowstone plume driven by subduction-induced mantle flow. *Nat. Geosci.* **6**, 395–399 (2013).
4. Leonard, T. & Liu, L. The role of a mantle plume in the formation of Yellowstone volcanism. *Geophys. Res. Lett.* **43**, 1132–1139 (2016).
5. Burdick, S. et al. Upper mantle heterogeneity beneath North America from travel time tomography with global and USArray transportable array data. *Seismol. Res. Lett.* **79**, 384–392 (2008).
6. Schmandt, B. & Humphreys, E. Complex subduction and small-scale convection revealed by body-wave tomography of the western United States upper mantle. *Earth. Planet. Sci. Lett.* **297**, 435–445 (2010).
7. Sigloch, K., McQuarrie, N. & Nolet, G. Two-stage subduction history under North America inferred from multiple-frequency tomography. *Nat. Geosci.* **1**, 458–462 (2008).
8. Sigloch, K. Mantle provinces under North America from multifrequency P wave tomography. *Geochem. Geophys. Geosyst.* **12**, Q02W08 (2011).
9. James, D. E., Fouch, M. J., Carlson, R. W. & Roth, J. B. Slab fragmentation, edge flow and the origin of the Yellowstone hotspot track. *Earth. Planet. Sci. Lett.* **311**, 124–135 (2011).
10. Tian, Y., Zhou, Y., Sigloch, K., Nolet, G. & Laske, G. Structure of North American mantle constrained by simultaneous inversion of multiple-frequency *SH*, *SS*, and Love waves. *J. Geophys. Res.* **116**, B02307 (2011).
11. Porritt, R. W., Allen, R. M. & Pollitz, F. F. Seismic imaging east of the Rocky Mountains with USArray. *Earth. Planet. Sci. Lett.* **402**, 16–25 (2014).
12. van der Lee, S. & Nolet, G. Seismic imaging of the subducted trailing fragments of the Farallon plate. *Nature* **386**, 266–269 (1997).
13. Zhou, Q., Liu, L. & Hu, J. Western US volcanism due to intruding oceanic mantle driven by ancient Farallon slabs. *Nat. Geosci.* **11**, 70–76 (2018).
14. Cao, A. & Levander, A. High-resolution transition zone structures of the Gorda slab beneath the western United States: implication for deep water subduction. *J. Geophys. Res.* **115**, B07301 (2010).
15. Schmandt, B., Dueker, K., Humphreys, E. & Hansen, S. Hot mantle upwelling across the 660 beneath Yellowstone. *Earth. Planet. Sci. Lett.* **331**, 224–236 (2012).
16. Gao, S. S. & Liu, K. H. Mantle transition zone discontinuities beneath the contiguous United States. *J. Geophys. Res. Solid Earth* **119**, 6452–6468 (2014).
17. Katsura, T. & Ito, E. The system Mg_2SiO_4–Fe_2SiO_4 at high pressures and temperatures: precise determination of stabilities of olivine, modified spinel, and spinel. *J. Geophys. Res.* **94**, 15,663–15,670 (1989).
18. Bina, C. R. & Helffrich, G. Phase transition Clapeyron slopes and transition zone seismic discontinuity topography. *J. Geophys. Res.* **99**, 15,853–15,860 (1994).
19. Deng, K. & Zhou, Y. Wave diffraction and resolution of mantle transition zone discontinuities in receiver function imaging. *Geophys. J. Int.* **201**, 2008–2025 (2015).
20. Wortel, M. J. R. & Spakman, W. Subduction and slab detachment in the Mediterranean–Carpathian region. *Science* **290**, 1910–1917 (2000).
21. Williams, Q. & Hemley, R. Hydrogen in the deep earth. *Annu. Rev. Earth. Planet. Sci.* **29**, 365–418 (2001).
22. Kohlstedt, D., Keppler, H. & Rubie, D. Solubility of water in the α, β and γ phases of $(Mg,Fe)_2SiO_4$. *Contrib. Mineral. Petrol.* **123**, 345–357 (1996).
23. Murakami, M., Hirose, K., Yurimoto, H., Nakashima, S. & Takafuji, N. Water in Earth's lower mantle. *Science* **295**, 1885–1887 (2002).
24. Wang, X.-C., Wilde, S. S., Li, Q.-L. & Yang, Y.-N. Continental flood basalts derived from the hydrous mantle transition zone. *Nat. Commun.* **6**, 7700 (2015).
25. Wei, S. S. & Shearer, P. M. A sporadic low-velocity layer atop the 410 km discontinuity beneath the Pacific Ocean. *J. Geophys. Res.* **122**, 5144–5149 (2017).
26. Dickinson, W. R. & Snyder, W. S. Geometry of triple junctions related to San Andreas Transform. *J. Geophys. Res.* **84**, 561–572 (1979).
27. Thorkelson, D. J. & Taylor, R. P. Cordilleran slab windows. *Geology* **17**, 833–836 (1989).
28. Wang, Y. et al. Fossil slabs attached to unsubducted fragments of the Farallon plate. *Proc. Natl Acad. Sci. USA* **110**, 5342–5346 (2013).
29. Piromallo, C., Becker, T. W., Funiciello, F. & Faccenna, C. Three-dimensional instantaneous mantle flow induced by subduction. *Geophys. Res. Lett.* **33**, L08304 (2006).
30. DeMets, C. & Merkouriev, S. High-resolution reconstructions of Pacific–North America plate motion: 20 Ma to present. *Geophys. J. Int.* **207**, 741–773 (2016).
31. Goff, J. A. & Cochran, J. R. The Bauer scarp ridge jump: a complex tectonic sequence revealed in satellite altimetry. *Earth. Planet. Sci. Lett.* **141**, 21–33 (1996).
32. Lynn, W. S. & Lewis, B. T. R. Tectonic evolution of the northern Cocos plate. *Geology* **4**, 718–722 (1976).
33. Anders, M. H. Constraints on North American plate velocity from the Yellowstone hotspot deformation field. *Nature* **369**, 53–55 (1994).
34. Muller, R. D. et al. Ocean basin evolution and global-scale plate reorganization events since Pangea breakup. *Annu. Rev. Earth. Planet. Sci.* **44**, 107–138 (2016).

Acknowledgements

This research was supported by the US National Science Foundation under Grants EAR-1737737 and EAR-1348131. Advanced Research Computing at Virginia Tech provided computational resources.

Competing interests

The author declares no competing interests.

Additional information

Supplementary information is available for this paper at https://doi.org/10.1038/s41561-018-0126-4.

Reprints and permissions information is available at www.nature.com/reprints.

Correspondence and requests for materials should be addressed to Y.Z.

Publisher's note: Springer Nature remains neutral with regard to jurisdictional claims in published maps and institutional affiliations.

Methods

I processed the broadband seismic data recorded at 550 USArray TA stations for earthquakes that occurred between January 2011 and January 2015 with magnitudes between 6.0 and 7.8. The epicentral distances of the events ranged from 45 to 90°. I used only shallow earthquakes with focal depths less than 100 km in this study to limit the interference between the depth phase (pP) and P-to-S converted waves (P410s and P660s) in the frequency band I investigated. For earthquakes shallower than 100 km, the dPs arrived within the first 25 s of the P-wave code, which can be modelled as part of the source process as the coda window used includes pP410 and pP660 waves, and those interactions are automatically accounted for in the calculation of finite-frequency sensitivity kernels. Aftershocks that occurred closely in time were also excluded from the study. This leaves an average of about 40 events at stations with a full deployment period of two years, and about 15 events for stations in the eastern part of the study regions (deployed shortly before 2011). Station locations and geographical distributions of the earthquakes are shown in Supplementary Fig. 1.

Receiver functions are calculated based on frequency-domain deconvolution using vertical and radial component P-wave coda seismograms. The time window starts at 20 s before the P-wave arrival and the length of window is 200 s, unless a PP wave arrives before the end of the window, in which case the PP arrival time defines the end of the time window. This limits the interference between Pds waves and PPds waves, which have different incident angles. A 20% time-domain cosine taper was applied to windowed seismograms before deconvolution. I calculated synthetic seismograms in a reference Earth model based on travelling-wave mode summation and applied the same data processing to generate synthetic receiver functions. The reference Earth model has a 35 km thick crust superimposed on a model IASP91 mantle. The transition-zone discontinuities in the reference model are at depths of 410 km and 660 km, respectively. I measured time differences between the observed and synthetic receiver functions using a 30 s cosine window centred at the reference arrival of the Pds phase. An example of the receiver function time-shift measurements is plotted in Supplementary Fig. 2. The observed and synthetic receiver functions show a general agreement in waveform at periods between 10 and 100 s. At periods shorter than 10 s, the observed receiver functions show strong structural noises (multiple scattering) that contaminate the Pds waves. To avoid strong multiple scattering, I filtered seismograms in the frequency domain with a flat response between the 10 and 100 s period. The 30 s cosine window used in the receiver function time measurements indicates that measurements at a 20 s period (0.05 Hz) represent frequency averaging roughly between 10 s (0.1 Hz) and 100 s (0.01 Hz).

A shallow seismic interface may generate multiple-reflected waves and those waves may arrive between the P410 and P660 phases. I excluded traces in which the P410 and P660 waves are contaminated by strong multiples. Finally, I excluded measurements beyond a 1.5 standard deviation to limit the impact of other uncertainties, such as hypocentre location and the focal mechanism of earthquakes. Overall, this leaves about 86% of the measurements in tomographic inversions.

Finite-frequency tomography. To image high-resolution discontinuity topography, I calculated the finite-frequency sensitivity for receiver function time measurements. The finite-frequency sensitivity kernels account for first-order wave-diffraction effects and therefore allow us to image small-scale features (in the order of a couple hundred kilometres) that are not resolvable in traditional ray-theory-based methods. Based on the Born scattering approximation, time shifts (δt) between the observed and synthetic P410s (or P660s) receiver functions can be written as a two-dimensional (2D) integration over depth perturbations (δd) on the seismic discontinuity Σ:

$$\delta t(\omega) = \iint_{\Sigma} K_t^d(\omega, \mathbf{r})\delta \mathrm{d}(\mathbf{r})\mathrm{d}\Sigma \quad (1)$$

I formulated the sensitivity kernel $K_t^d(\omega, \mathbf{r})$ in the framework of the travelling-wave-mode coupling and fully accounted for the spectral division as well as interactions of all possible phases arriving in the P-wave coda, including PcP and pP waves. Here, ω is the angular frequency and $\mathbf{r}$ is the position vector. Examples of finite-frequency sensitivity to depth perturbations of the 410 km and 660 km discontinuities are given in Supplementary Fig. 3. The topography models are parametrized into 0.5°×0.5° grid points and I assumed that depth variations can be determined by linear interpolation using four-corner grid points in latitude–longitude cells. Sensitivity kernels were calculated at much denser grids to ensure integration accuracy. The depth perturbations in equation (1) are solved in a regularized least-square inversion:

$$\|G\mathbf{m}-\mathbf{d}\|^2 + \alpha^2 \|\mathbf{m}\|^2 = \text{minimum} \quad (2)$$

where G is the kernel matrix, $\mathbf{m}$ is the model vector and α is the Tikhonov regularization parameter.

The minimization problem leads to:

$$(G^T G\mathbf{m} - G^T d) + \alpha^2 \mathbf{m} = 0 \quad (3)$$

The superscript T denotes the transpose of a matrix. I solve the above inverse problem based on the singular value decomposition of the $n \times m$ matrix G:

$$G = U\Sigma V^T \quad (4)$$

Matrices U and V contain left and right singular vectors, $\mathbf{u}$ and $\mathbf{v}$, respectively. The singular value matrix $\boldsymbol{\Sigma}$ is a rectangular diagonal matrix with an upper $m \times m$ diagonal matrix and a lower zero matrix. The Tikhonov solution of the inverse problem can be written as

$$\mathbf{m} = \sum_{j=1}^{p} \left(\frac{\sigma_j^2}{\sigma_j^2 + \alpha^2} \right) \frac{\mathbf{u}_j^T \mathbf{d}}{\sigma_j} \mathbf{v}_j \quad (5)$$

where p is the rank of the singular value matrix. The corresponding resolution matrix is:

$$R = VFV^T \quad (6)$$

where F is a diagonal matrix with elements $\sigma_j^2 / (\sigma_j^2 + \alpha^2)$, and σ_j is the jth singular vector. Trade-off curves, kernel densities as well as diagonal elements of the resolution matrix R for the the 410 and 660 models in Fig. 2 are plotted in Supplementary Figs. 4 and 5.

Wave-speed and crustal corrections. In addition to discontinuity depth variations, mantle wave-speed perturbations as well as 3D crustal structure can introduce time shifts on P410s and P660s receiver functions. I corrected receiver-function time measurements based on 3D finite-frequency P-wave[8] and S-wave[10] models. In general, time corrections based on mantle wave speed and crustal structure do not change the overall structure of the perturbations. This is because receiver functions reflect the relative timing between P waves and P-to-S converted waves, which is less sensitive to wave-speed structures when P-wave and S-wave perturbations are highly correlated. On average, the upper mantle is slower than the global average and the MTZ is colder than the global average in this region. The corrections reduce the mean P410 and P660 delay times by 0.21 and 0.16 s, respectively. Crustal corrections are calculated using a global crust model CRUST1.0 (ref. [35]). Crustal thickness in most of the region is between 30 and 40 km (35 km in the reference model) and calculated corrections are less than 0.15 s, except for in the Rocky Mountains where crustal thickness reaches about 52 km, which corresponds to 0.45 s in crustal correction. The average P-wave and S-wave speed in the upper mantle and the MTZ, as well as in the 410 km and 660 km discontinuity models with and without those corrections are plotted in Supplementary Fig. 7.

Code availability. The GMT software package used to prepare Figs. 1 and 2 is available here www.soest.hawaii.edu/gmt/.

Data availability. Seismic data used in this research are available from the IRIS Data Management Center (www.iris.edu).

References

35. Laske, G., Masters, G., Ma, Z. & Pasyanos, M. Update on CRUST1.0—a 1-degree global model of Earth's crust. *EGU General. Assem. Conf. Abstr.* **15**, 2658 (2013).